PAPER • OPEN ACCESS

Laminography in the lab: imaging planar objects using a conventional x-ray CT scanner

To cite this article: S L Fisher *et al* 2019 *Meas. Sci. Technol.* **30** 035401

View the article online for updates and enhancements.

Laminography in the lab: imaging planar objects using a conventional x-ray CT scanner

S L Fisher[1], **D J Holmes**[1], **J S Jørgensen**[2,3], **P Gajjar**[2], **J Behnsen**[2], **W R B Lionheart**[3] **and P J Withers**[2,4]

[1] School of Physics and Astronomy, The University of Manchester, Manchester, M13 9PL, United Kingdom
[2] Henry Moseley X-Ray Imaging Facility, School of Materials, The University of Manchester, Manchester, M13 9PL, United Kingdom
[3] School of Mathematics, The University of Manchester, Manchester, M13 9PL, United Kingdom
[4] Henry Royce Institute, The University of Manchester, Oxford Road, Manchester, M13 9PL, United Kingdom

E-mail: p.j.withers@manchester.ac.uk

CrossMark

Abstract
Whilst x-ray micro-computed tomography (CT) machines have developed into a popular laboratory tool for non-destructive 3D imaging of materials, they are not well-suited for scanning flat objects, for which there is an increasing demand. Computed laminography (CL) techniques have been developed for imaging planar samples such as fossils, paintings, printed circuit boards and composite panels. This paper is the first work demonstrating how CL may be implemented on a conventional industrial laboratory micro-CT scanner, without the need for specialist equipment. A rotary CL scan configuration (also known as tilted or oblique CT) was successfully implemented, and the projection images reconstructed using the conjugate gradient least squares (CGLS) method. Computer simulations were used to analyse the causes of image artefacts seen in the cone-beam CL reconstructions, and to devise corrections for them. The resulting laboratory CL method produces reconstructions with fewer artefacts and a more isotropic resolution compared to limited-angle scan configurations otherwise used for planar samples. This demonstrates that CL can be performed in the laboratory without specialist equipment beyond that required for standard CT[5].

Keywords: x-ray imaging, laminography, rotary laminography, x-ray computed tomography (XCT)

(Some figures may appear in colour only in the online journal)

1. Introduction

In many different academic disciplines and industrial applications, recording and analysing the internal structure of materials non-destructively is of paramount importance. One commonly used technique is x-ray computed tomography (CT), where a finite number of radiographic projection images are acquired as the object is rotated with respect to an x-ray source and detector. These projections are then mathematically reconstructed to produce a virtual 3D volume that reveals the structural characteristics of the object in the form of attenuation contrast.

CT has been incredibly successful at determining the internal 3D structure of objects in a variety of fields such as medical sciences [1], engineering [2, 3] and geology [4]. However, there is now an increased demand for the visualisation of flat objects such as paintings [5], printed circuit boards (PCBs) [6], fossils [7], and composite panels in the aerospace industry [8]. Unfortunately, conventional CT techniques are
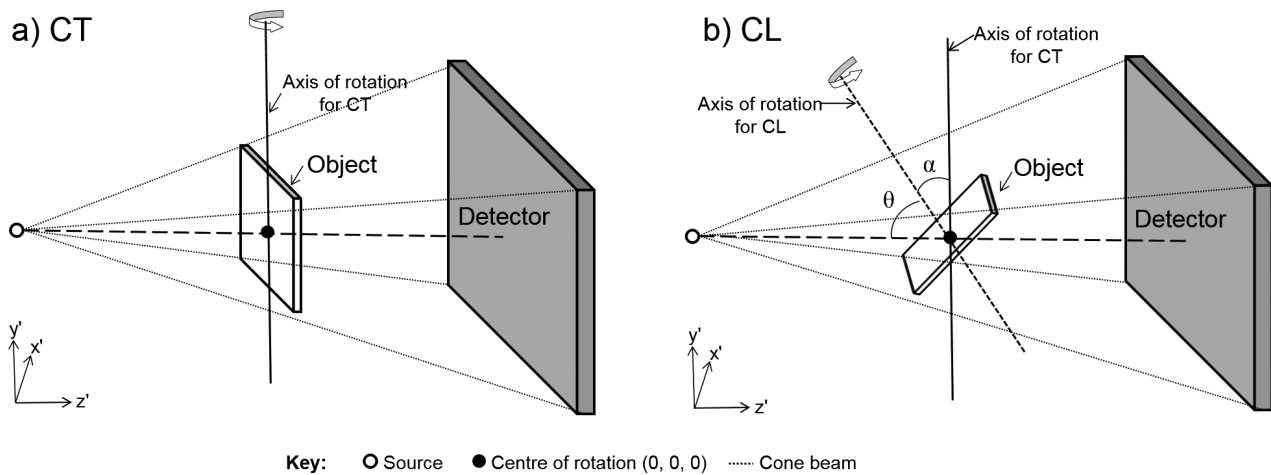
Figure 1. Schematic diagram showing (a) a conventional circular scan CT setup, and (b) our laminography (CL) setup.

not well-suited to scanning such laterally extended planar objects without incurring significant image artefacts. One reason for this is that the large aspect ratio of planar samples leads to extensive x-ray path lengths through the sample at certain projection angles (along the object plane), preventing any usable x-ray transmission. In other cases, the large size of the objects may prevent a full 360° rotation. Although the projection images can be reconstructed with projections at certain angles missing, there are often severe (limited-angle/missing-wedge) image artefacts which degrade the image quality, due to missing information from the angles not scanned or sub-optimally acquired.

A number of alternative techniques have been developed for scanning flat planar objects, which together are known as computed laminography (CL) [9, 10]. One specific case that is the focus of this work is rotary laminography, where the rotation axis of the sample is tilted at an angle of less than 90° to the horizontal (hence it is also known as tilted or oblique CT). This tilting of the rotation axis means that similar x-ray transmission through the sample can be obtained at all projection angles. Furthermore, the tilting increases the effective field of view of the detector, therefore allowing larger objects to be scanned. CL is a subset of CT in its widest sense of reconstructing a volume from projection images in any geometric configuration. However for the remainder of this paper, we follow the convention of [11] in referring to CT as the most popular geometric configuration of the sample rotating about an axis orthogonal to the beam propagation direction. By the same convention we refer to CL as specifically rotary laminography. Thus in short, the main difference of CL to CT is the tilted rotation axis.

Compared to other laminography methods, rotary laminography is the simplest to implement for non-movable source and detectors, as is the case with synchrotron facilities and many conventional CT machines. For this reason, it has been the method of choice at several synchrotron beamlines [9, 12–15] and has been used successfully to examine fossils [16], polymer composite failure [17] and paintings [18]. In the laboratory, laminography has been developed using hexapods and robotic arms [19–21]. However, to the knowledge of the

authors, standard laboratory CT machines have not been used for any type of laminography.

This paper is the first work demonstrating how computed laminography may be implemented on a conventional industrial laboratory micro-CT scanner, without the need for specialist equipment. A method is presented for scanning a flat test object using rotary laminography, and reconstructed using the iterative conjugate gradient least squares (CGLS) algorithm. Simulations have been performed to characterise and help devise correction methods for a number of artefacts found in the raw reconstructed data. The achievable image quality of the laminography method is assessed against a comparable limited-angle CT scan and shown to produce images with more isotropic resolution and less artefacts, in particular within the object plane.

2. Experimental setup

2.1. Conventional micro-CT configuration

Most conventional micro-CT machines that are used for industrial and material science applications in the laboratory have a fixed point x-ray source and a fixed or translatable detector. As shown in figure 1(a), the beam emanates from the source as a cone whose central ray is incident normal to the plane of the detector. Relative motion between the source and the sample creates a number of projection images, which can produce a stable reconstruction depending on the source-sample path [22, 23]. Rotating the sample about an axis perpendicular to the central x-ray path is attractive due to its mechanical simplicity, with the rotation axis usually vertical for physical stability.

In the laboratory reference frame ($x'y'z'$), the z' axis points along the beam direction and the y' axis is vertical. The x' direction is perpendicular to y' and z' as shown in figure 1. In the object reference frame (xyz), the z axis is normal to the surface of the object and x and y are in the plane of the object. In CT, the y axis is parallel to the y' axis, and in CL, the z axis is parallel to the axis of rotation shown in figure 1(b).

During a standard CT scan, the object is rotated through 360° with projections taken at equi-angular increments. This
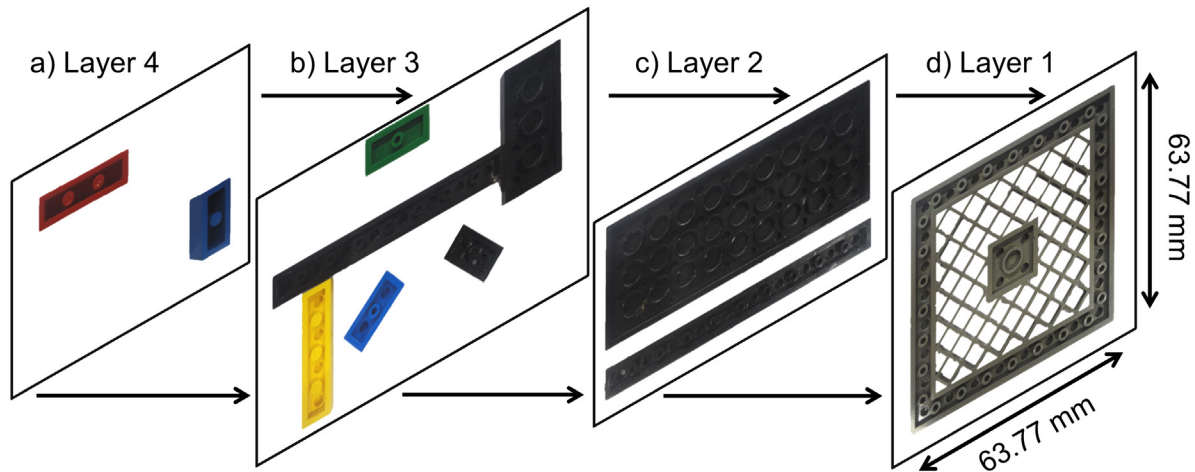
Figure 2. The four layers of the Lego test sample, as scanned using the laminography method. The arrows show how the sample was constructed.

method is most efficient for cylindrically shaped samples, but is non-optimal for flat planar objects.

2.2. Laminography implementation

To implement a laminography scan, the object was placed in between the x-ray source and a detector, with the manipulator arm tilted so that the axis of rotation was at an angle of $\alpha = 30°$ to the vertical, as shown in figure 1. As with conventional CT, the sample was rotated through 360°, but about the tilted axis, and projection images were recorded at equiangular intervals.

This work utilised a Nikon XTEK XTH 225 cabinet system, which comprises a 225 kV micro-focus source, a fixed Varian 4030E flat-panel detector of size 3192 × 2296 pixels and a 5-axis manipulator arm that allows the sample to be moved in all three spatial dimensions, rotated through 360° and tilted to a maximum of $\alpha = \pm30°$ to the vertical. It is this tilt facility that allowed rotary laminography to be implemented. However, the instrument does not natively support scanning with a tilted rotation axis, only allowing a standard circular CT scan. Instead, the IPC interface to the proprietary Nikon Inspect-X software [24] gives flexibility for automating acquisition from non-standard geometries [25], and was exploited to create a circular scan routine with a tilted rotation axis.

2.3. Sample details

For the purpose of evaluating the laminography method, a planar test object was constructed using Lego blocks (a construction toy made from acrylonitrile butadiene styrene [26] that is manufactured by 'The Lego Group'). Lego blocks are made to a high tolerance of 10 μm [27] and were used to create an accurately defined structure against which the reconstructions can be compared to identify artefacts. The Lego test object is illustrated in figure 2. The sample has a similar thickness to PCBs and fossils, and the transmission through the shortest edge is predicted to be at least three times that of the
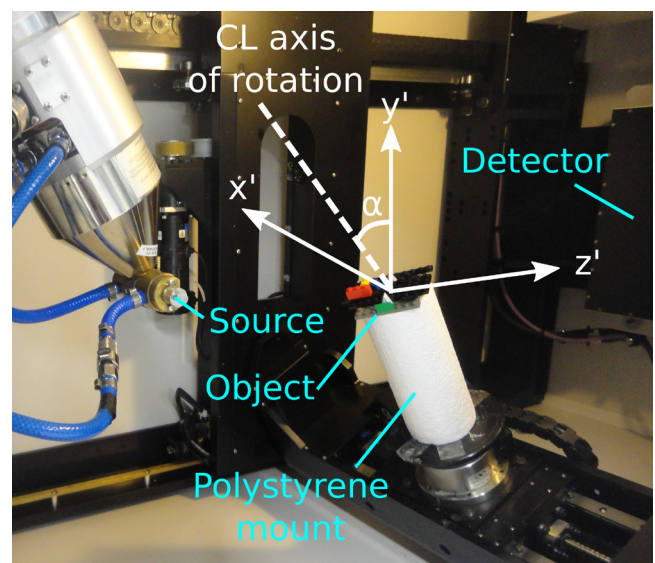
Figure 3. The Nikon XTH 225 cabinet system set up for laminography of the test object.

long edge. Together with the internal structure, this makes it a suitable sample for this proof of concept study. As shown in figure 3, the object was mounted on the stage of the CT scanner using an expanded polystyrene cylinder.

2.4. Laminography scan parameters

The Inspect-X interface and IPC code was used to perform a rotary laminography scan with the sample titled at 30° towards the x-ray source. The sample was rotated through 360° with 2513 projection images acquired at equispaced angles. This number of projections was suggested by the Nikon proprietary software based on the Nyquist sampling frequency theorem from the projection image size. The projection images were binned by a factor of 2 to produce 1596 × 1148 pixel projection images with a physical pixel size of 0.254 mm. The geometric magnification was 2.8. The voltage was set to 80 kV,

the current was 85 μA and the exposure time for each projection image was 250 ms.

2.5. Limited-angle CT scan

In order to evaluate the performance of the laminography method a limited-angle CT scan of the same sample was acquired. One of the blocks in layer four was removed (the block on the right in figure 2(a)) so that the sample could stand upright on a foam mount. A standard circular CT scan was acquired with 2513 projections and the same scan parameters as in section 2.4. The projection images in the angular ranges $0° \pm 30°$ and $180° \pm 30°$ were removed from the data set, as this was where the rays were travelling through the long edge of the object causing a substantial reduction in transmission.
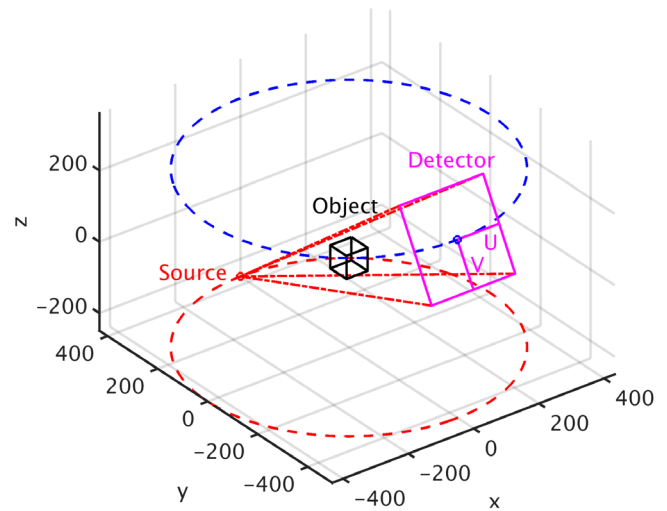
3. Reconstruction method

3.1. The reconstruction problem and method

Once a set of projection images is obtained the next step is to reconstruct a virtual volume of the object. Conventionally, reconstruction of cone-beam CT data is carried out using the analytical Feldkamp–Davis–Kress (FDK) method [28], due to simplicity and computational speed. However, standard implementations of FDK assume a simple circular (non-tilted) scan trajectory. In particular, this is the case in the commercial reconstruction software provided with the Nikon XTH 225 cabinet system used in the present work, thus precluding laminography. While in principle FDK can be generalised to the rotary laminographic trajectory, a modified filter is needed to take the tilt into account [29]. A software implementation of FDK allowing this was not readily available to the authors. Another way of reconstructing laminography data is to convert projection images from the detector onto a virtual tilted detector. The 'virtual' projection images can then be reconstructed using standard FDK. However this technique naturally incurs interpolation errors and therefore was not used in this work.

Iterative reconstruction algorithms provide an extremely flexible alternative to conventional analytical reconstruction methods such as the FDK method, since they can be directly applied to any non-standard acquisition geometry such as in laminography. To set the stage for iterative reconstruction, the reconstruction problem is formulated as a system of linear equations,

$$W v \simeq p, \tag{1}$$

where v is a vector of length n representing the object voxel values, W is a $m \times n$ matrix called the system matrix describing how the rays intersect the voxels, and p is a vector of length m representing the projection data after flat-field and negative-logarithm correction required by the Beer–Lambert model. The values m and n correspond to the product of the number of projections and the number of detector pixels, and the number of voxels in the reconstruction volume,

Figure 4. The path of the source and detector during the scan in the object's frame of reference *xyz*.

respectively. The data p is measured by the detector, and the elements of W can be found using ray tracing [30].

To determine a 3D reconstruction of the object, the linear system in (1) must be solved for v, i.e. the values of all voxels in the volume. Due to noise and other imperfections during acquisition an exact solution to (1) cannot be expected and instead the problem is reformulated as a least-squares problem. Due to the large data size an iterative method must be used to solve the problem.

In this work the conjugate gradient least squares (CGLS) method [31] is employed. The CGLS algorithm was chosen due to its fast convergence rate. While non-negativity cannot be enforced by the CGLS algorithm, non-negativity was tested with the simultaneous iterative reconstruction technique (SIRT) algorithm [32, 33]. However only a marginal improvement was observed and the faster convergence rate of CGLS was preferred. The SIRT results have been omitted for brevity.

One hundred iterations of the CGLS algorithm were run to reconstruct the experimental data. This number was determined by visual inspection of the resulting images to be the number that produced an image that is sharp but with low noise, obtained in a reasonable time. Running for more than 100 iterations would not only take an excessive amount of time, but also decrease the image quality due to the introduction of noise [34].

3.2. Implementation details

To fully specify the problem in (1) the system matrix W specific to the considered laminographic setup must be established. Due to the large data set it is not feasible to explicitly store the matrix in computer memory, even in sparse matrix format; instead we rely on a matrix-free implementation computing the matrix values on the fly when needed during the CGLS algorithm. This is accomplished using the ASTRA Tomography Toolbox (version 1.8 for MATLAB) [35, 36]
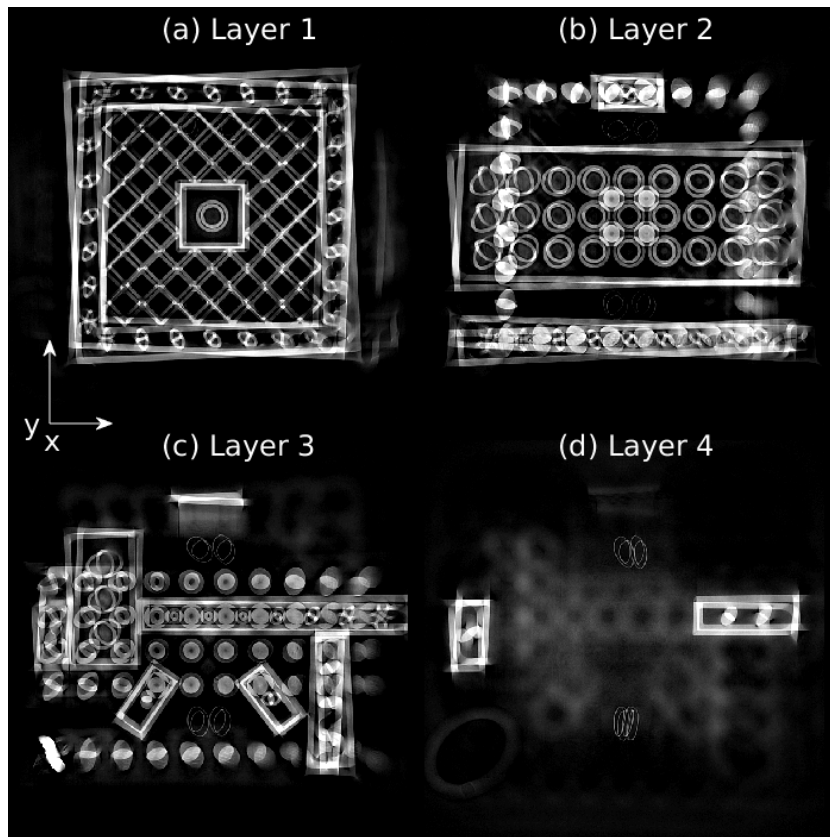
Figure 5. A 3D reconstruction of the Lego test sample was performed using the laminography method with no image corrections. (a)–(d) are sections through this reconstruction volume in the *xy* plane, corresponding to the layers of the sample shown in figure 2.

which offers GPU-accelerated application of the system matrix and its transpose.

In order for the system matrix W to be computed, the relationship between the source, detector and object in each projection image must be known. In ASTRA this is done using vectors specifying the source and detector positions at projection angle ϕ_i, S_i and D_i respectively, and two perpendicular unit vectors U_i and V_i, which specify orientation and size of the detector pixel array at projection angle ϕ_i. The S_i, D_i, U_i, and V_i position vectors are given in the object's frame of reference by convention, where the centre of rotation lies at the origin. For the laminography setup considered here, the position vectors are described using the following equations:

$$S_i = (-s\sin\theta\sin\phi_i, s\sin\theta\cos\phi_i, -s\cos\theta), \quad (2)$$

$$D_i = (d\sin\theta\sin\phi_i, -d\sin\theta\cos\phi_i, d\cos\theta), \quad (3)$$

$$U_i = (p\cos\phi_i, p\sin\phi_i, 0), \quad (4)$$

$$V_i = (\Delta p\cos\theta\sin\phi_i, -\Delta p\cos\theta\cos\phi_i, -\Delta p\sin\theta), \quad (5)$$

where s is the source-to-object distance, d is the detector-to-object distance, α is the tilt angle of the rotation stage, Δp is the detector pixel size and $\theta = 90° - \alpha$. These equations were adapted for the coordinate system used in this work from the vectors used in [35]. All dimensions are given in units of voxels.

It can be seen from equations (2)–(5) that the position vectors are transformed into the object's frame of reference by

applying two rotations. The first is a rotation about the x' axis by an angle θ as measured from the z' axis. The second is a rotation about the CL rotation axis by the projection angle at projection i, ϕ_i. A visual representation of vectors U and D at an arbitrary projection angle can be seen in figure 4.

3.3. Raw reconstruction result

Despite ASTRA's GPU-acceleration, the laminography reconstruction of the test sample, using 2513 projection images of size 1596×1148 took several hours[6] to complete. To speed up proof-of-concept studies, projection images were further reduced in size to 798×798 pixels so that the reconstruction time could be reduced. This was achieved by binning the 1596×1148 projection images by a factor of 2, and padding to make the images square.

The result of running 100 iterations of the CGLS algorithm on this reduced-size projection dataset obtained from scanning the test object using the laminography method is shown in figure 5. The test sample layers are clearly identifiable, however severe reconstruction artefacts are apparent. In layer 1, figure 5(a), the lines of the grid are shadowed by further copies of the same line that diverge from the centre of the image. In layer 2, figure 5(b), the circles of the central grid have elliptical shadows. In both layers, the artefacts are worse further from the centre of the image. Similar artefacts can

---

[6] Running on a computer with a 3.10 GHz Intel Xeon E5-2687W v3 processor, 256 GB RAM and a NVidia Quadro K6000 GPU.
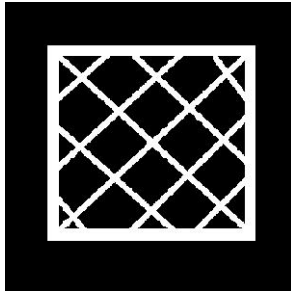
Figure 6. The central slice (slice 150) of the phantom volume used to identify sources of artefacts in laminography.

be seen in the other layers of the image, figures 5(c) and (d). These artefacts have a number of potential causes such as geometrical misalignments, scanning parameters being measured incorrectly, and also the scanning geometry itself. In standard CT, artefacts can be reduced or removed by applying corrections prior to the reconstruction process [37]. However, in CL, and in particular laboratory cone-beam CL, the causes of artefacts and how to correct for them is not well documented in the literature. For this reason we consider the most important of these artefacts as well as methods for their correction.

4. Artefact characterisation and correction

Computer simulations were performed to simulate different types of artefacts found in a typical CL image. The origin of some of these artefacts is the same as in CT but the artefact could appear differently in laminography reconstructions due to the difference in geometry. The phantom chosen for simulations was a thin (3 pixel thick) grid phantom, as shown in figure 6. This was chosen to resemble the grid used in layer 1 of the Lego sample. The phantom volume was $300 \times 300 \times 300$ voxels. The grid and surrounding volume were assigned relative attenuation values of 1 and 0 respectively.

We consider a laminography geometry with tilt angle of the rotation stage $\alpha = 30°$, source-to-object distance $s = 500$ mm and detector-to-object distance $d = 900$ mm, which we refer to as the *standard geometry* and which is comparable to the geometry used in the Lego test object scan. An artefact was simulated by creating projection images using a geometry with one parameter slightly different to the standard geometry and then reconstructing with the standard geometry.

The geometry differences were made by changing one parameter in turn:

　(i) the position of the centre of rotation,
　(ii) the source-to-object distance s, and
　(iii) the tilt angle α of the rotation stage.

Intrinsic laminography artefacts [38], the artefacts that appear even when both projection and reconstruction geometries are the same, were also investigated.

The aim of the simulations was to identify the origin of different artefacts and devise effective tools for the correction of the experimental data.
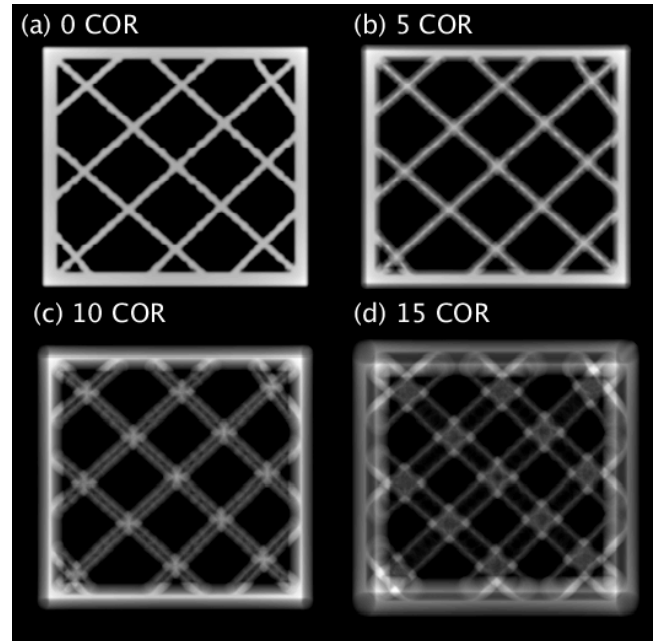
Figure 7. The effect of a displacement of the centre of rotation in the x' direction. Reconstructions of the central slice of the phantom are shown for the lateral displacement of the COR by (b) 5 pixels, (c) 10 pixels and (d) 15 pixels in the x' direction from the central line in the simulated projection image. Compare this to the reconstruction with no displacement in (a).

4.1. Incorrect centre of rotation

During reconstruction it is assumed that the centre of rotation (COR) of the sample lies on the line connecting the source and the centre of the detector. However in practice, it is common for the COR to be slightly to the left or right of this line in the x' direction. To model this, projection images were simulated using the standard geometry, and pixels were added to the right hand side of each simulated projection image to shift the centre of the image. The data was reconstructed using the standard geometry assuming no COR shift. This was found to cause doubling of the edges in the image uniformly across the image, as is the case in standard CT [37]. This effect increases with larger COR displacements from the central line, as shown in figure 7. COR shifts in either direction along the x' axis give the same effect.

A simple COR correction was implemented by computationally adding columns to the right or left hand side of each projection image. The number of columns that needed to be added was determined manually by reconstructing using a range of different corrections, then comparing all the different resulting images to decide which correction produced the optimal image.

4.2. Incorrect laminography tilt angle

The effect of an inaccurate measurement of the laminography tilt angle was investigated using the grid phantom. The simulated projection data was generated using tilt angles α between 25 and 35°, so as to simulate an error in the tilt angle
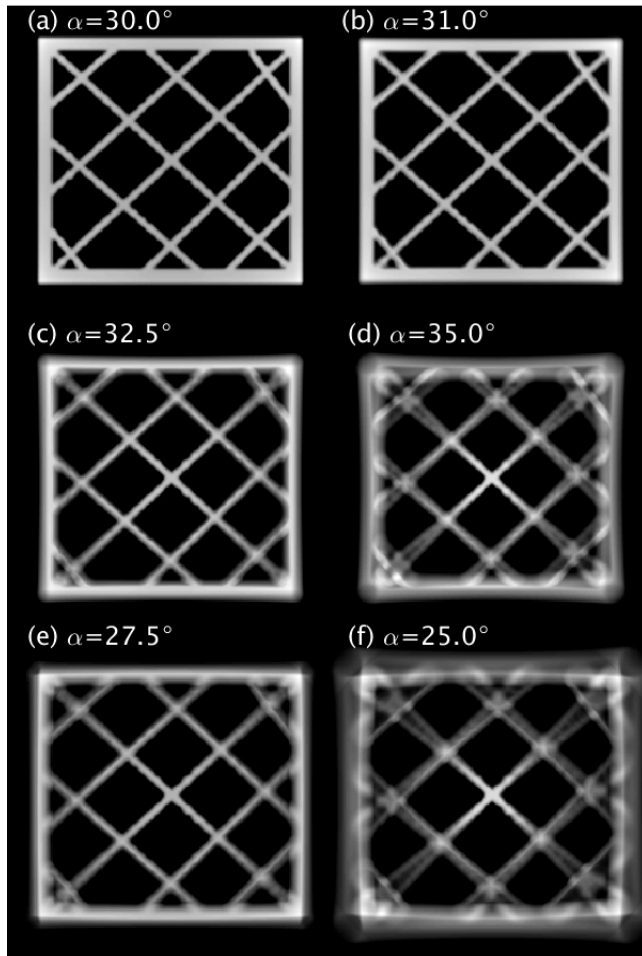
**Figure 8.** Simulated reconstructions (using $\alpha = 30°$) of projection data with (a) $\alpha = 30.0°$, (b) $\alpha = 31.0°$, (c) $\alpha = 32.5°$, (d) $\alpha = 35.0°$, (e) $\alpha = 27.5°$ and (f) $\alpha = 25.0°$. This shows an error in the tilt angle produces an artefact that gets worse as the error increases.

measurement by up to $\pm 5°$. As seen in figure 8, the error in the tilt angle causes the lines in the grid to diverge. Lines with larger radial distance from the centre of the image experience a greater divergence. As the difference between α and 30° increases, the lines start to diverge closer to the centre, and the rate of divergence is more rapid along the radial direction. The blurring caused by the diverging lines lies on the inner edge of the line when $\alpha > 30°$, and on the outer edge when $\alpha < 30°$. As a result, reconstructions with $\alpha < 30°$ appear larger than images with $\alpha > 30°$ due to blurring around the outer edges of the grid.

To reduce this error, the actual laminography tilt angle can be determined accurately by using a single projection at projection angle $\phi_0 = 0°$. The length of the object in the vertical direction on the projection image can be measured by considering the magnification of the scan compared to the actual size of the object along that same dimension. Using these two distances, the tilt angle can be computed as

$$\alpha = \arccos\left(\frac{l_{\text{proj}}}{l}\right), \tag{6}$$
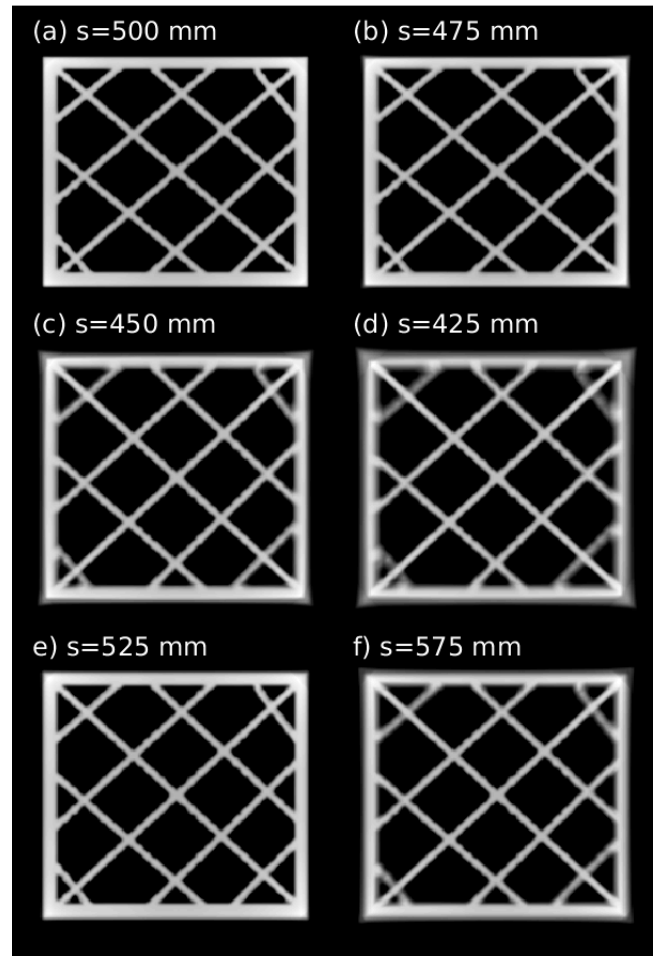
Figure 9. Projection images were created with different source-to-object distances, s, and reconstructed using the standard geometry. Reconstructions of the central slice of the phantom are shown for (a) $s = 500$, $d = 900$ mm (no change from standard), (b) $s = 475$, $d = 900$ mm, (c) $s = 450$, $d = 900$ mm, (d) $s = 425$, $d = 900$ mm, (e) $s = 525$ mm, $d = 900$ mm and (f) $s = 575$ mm, $d = 900$ mm.

where l is the true length of the object, and l_{proj} is the length of the object as measured on the projection image at 0°.

4.3. Incorrect source-to-object distance

A mismatch between the source-to-object distance in the projection and reconstruction geometry can also cause image artefacts. To identify the effect of the error we created, projection images with different source-to-object distances from the standard were made and reconstructed using the standard geometry described in section 4. Figure 9 shows the results of this simulation.

The artefact is worse the greater the difference between the source-to-object distance, s, used in reconstruction from that used to create the projection images. For example in figures 9(c) and (d), where s is 50 mm and 75 mm less than the standard respectively, there is visible blurring to image lines on the outer edges of the grid. This blurring increases with increasing radial distance from the centre of the image. Unsurprisingly, the artefact worsens the greater the error in s.
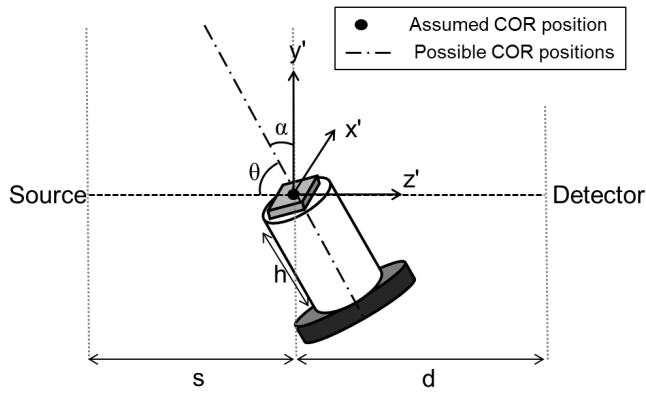
Figure 10. Schematic of the laminography setup. The centre-of-rotation is assumed to lie on top of the mount, as indicated by the figure. Misalignments in the scanner can mean it could lie at any point along a line of points at an angle α to the y' axis.

The effect is also noticeable for s greater than the standard, as shown in figures 9(e) and (f).

Accurately determining the distance between the x-ray source and centre of the object proves a complex task. As shown in figure 10, when the object is tilted to an angle α to the vertical, the source-to-object distance decreases by $h \sin \alpha$ where h is the height of the polystyrene mount. However, this assumes that the COR of the object and mount as they are tilted to the specified tilt angle lies at the base of the mount. Depending on the x-ray scanning system that is being used, this may not be the case and this centre of rotation may lie above or below the mount. This is illustrated in figure 10.

There are several contributions to an error in the source-to-object distance in laminography. There are alignment errors of the CT machine which are typically of the order 1–10 mm. An error in the measurement of the mount height, h, will also contribute to an error in s. The largest source of error contributing to an error in s is the error in the position of the centre-of-rotation, which could be of the order $h \sin \alpha$. In this work, $h = 140$ mm and $\alpha = 30°$, hence the error could be of the order 70 mm.

One method to accurately determine the source-to-object distance is to once again use a projection image of the object at $\phi_0 = 0°$. This time, the width of the object in the centre of the image across the horizontal plane can be used to determine the source-to-object distance using the following equation,

$$s = \frac{dw}{w_{\text{proj}}}, \qquad (7)$$

where s and d are the source-to-object and source-to-detector distances respectively, w is the real width of the object and w_{proj} is the width of the object in the projection image taken at 0°.

4.4. Intrinsic laminography artefacts

Just like in limited-angle CT, the geometry of laminography does not allow a complete data set to be acquired in the sense of admitting exact mathematical reconstruction, as information is missing in certain directions.
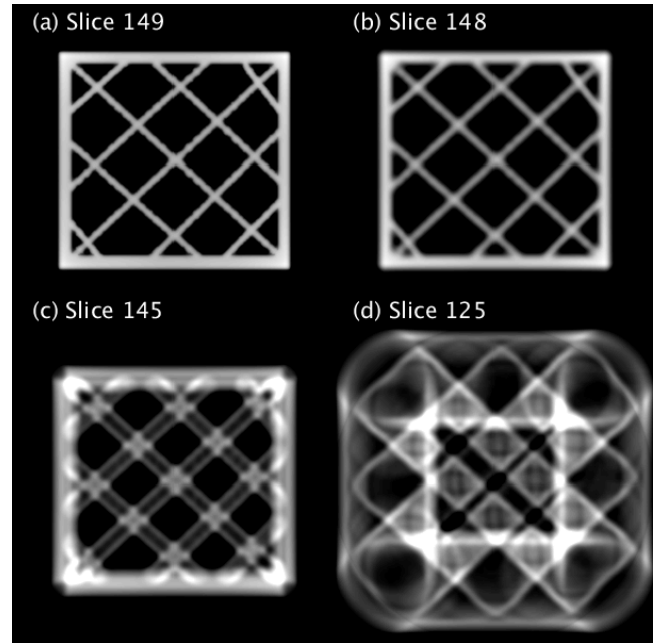
Figure 11. Slices through the *xy* plane of the reconstructed grid phantom. The phantom is 3 pixels thick and lies between slices 149 and 151, however an image is seen in slices 145 and 125 due to intrinsic laminography artefacts.

This missing information causes intrinsic laminography artefacts, as described in [38] for the parallel-beam case. To demonstrate this in the simulation, the projection images for the grid phantom were simulated and reconstructed using the same geometry. Figures 11 and 12 show the reconstruction in the *xy* and *yz* planes respectively. The artefact pattern is the same in both the *yz* and *xz*, appearing as white lines that streak across the image at an angle α to the *z* axis.

In the *xy* plane, these artefacts mean that the object appears thicker than it is. For example, the grid phantom is only 3 pixels thick, and, with each slice being 1 pixel in thickness, should only be visible in slices 149–151 in the *xy* plane. However, shadows of the object are still visible even up to slice 125, as shown in figure 11. The shadows become increasingly blurred the further away from the central slice the slice is taken.

4.5. Applying corrections to experimental data

The artefacts in the raw reconstruction of the Lego test object, as shown in figure 5, were compared to the simulation results in sections 4.1–4.4, and the derived corrections were applied. In cases where user-input was necessary to determine the correct value, for example when implementing a COR correction, a reconstruction was run using 10% of the projection images, evenly sampled from the data set, and run for 25 CGLS iterations.

5. Results and discussion

Reconstruction of the full laminography Lego test object dataset, with all corrections applied was obtained by 100 CGLS iterations, and is shown in figures 13 CL and 14 CL.
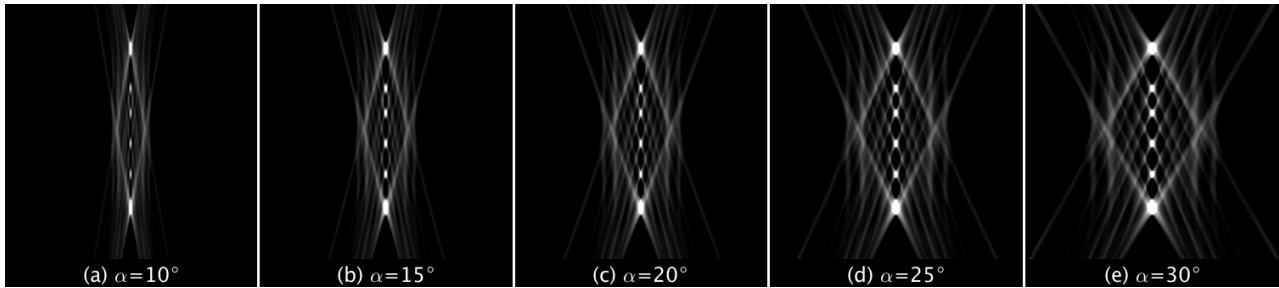
Figure 12. Laminography reconstructions of the grid phantom in figure 6, each time using a different laminography tilt angle. The reconstruction of slice 134 through the 3D volume in the yz plane is shown for (a) $\alpha = 10°$, (b) $\alpha = 15°$, (c) $\alpha = 20°$, (d) $\alpha = 25°$ and (e) $\alpha = 30°$.
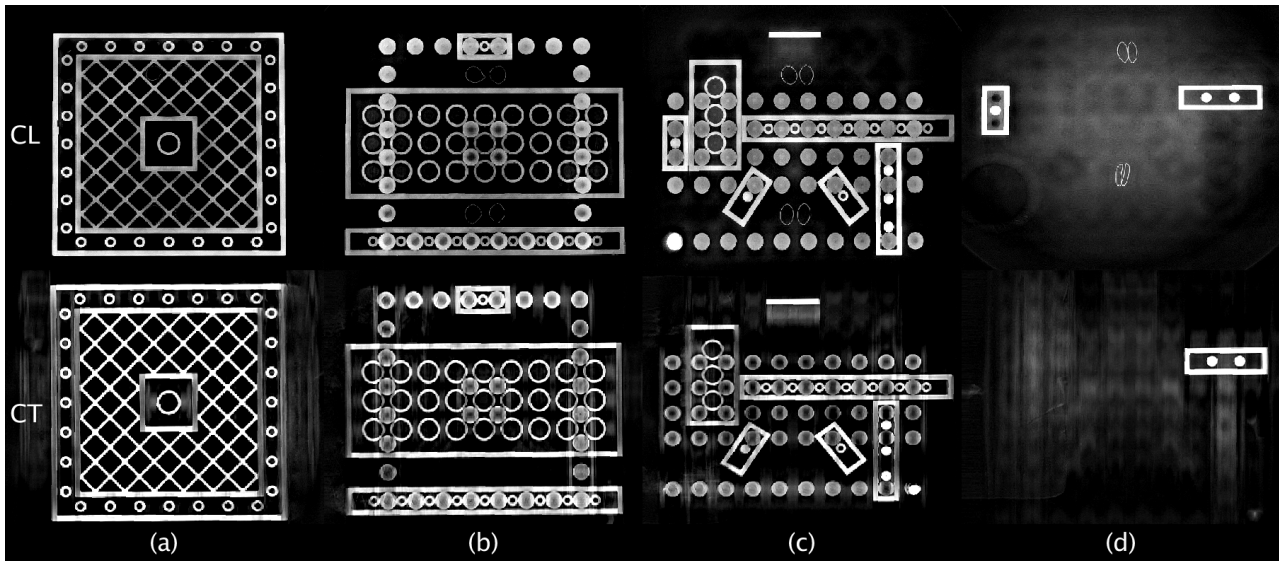
Figure 13. Reconstructions of layers 1–4 of the test object using the CL method and the limited-angle CT method (CT). The images shown are slices through the reconstruction volume in the xy plane.

It is evident that the geometric artefacts of figure 5 have been greatly reduced, and only intrinsic artefacts now significantly effect the image quality.

Reconstructions in the xy plane have homogeneous intrinsic artefacts, which originate from the centre of the image. These artefacts become more prominent in slices further from the central slice; in the central slice, as shown in figure 13 CL (a), the artefact appears as a slight darkening of the image around the centre, whereas further out from the centre, for example in figure 13 CL (d) the artefact is a large white haze around the centre. Features of other layers of the slice below the current slice can be seen, although blurred, within this artefact. This agrees with what was seen in the simulations in this work, and also with the work by Xu *et al* [38] using a synchrotron beam.

In the yz and xz planes, artefacts appear as streaks in the direction of the missing information. The angle of the streak artefacts with respect to the z axis depends on the tilt angle used in the laminography scan. The artefacts have an identical appearance in both planes, highlighting the homogeneity of the intrinsic artefacts in the xy plane. This is the same intrinsic laminography artefact that was seen in simulation (figure 12) and also agrees with the literature [38].

To compare the laminography method with the limited-angle CT method, the circular CT scan data set (with projections in

angular ranges $0° \pm 30°$ and $180° \pm 30°$ removed) was used. It was reconstructed using 100 CGLS iterations and a standard CT projection geometry. Only a COR correction was applied in this case, following the same procedure as for the laminography case. The result is shown in figures 13 CT and 14 CT.

The artefacts produced in the reconstruction of the limited-angle CT scan data differ from those observed in the laminography reconstruction, appearing as streaks along the y direction in the xy plane. In the yz plane, streak artefacts appear at an angle to the z axis related to the angle of missing information, similar to those seen in the laminography case. However, in the xz plane, the manifestation of artefacts is different; edges of the object appear blurred and contain streaks which show the blurred outline of previous layers of the object.

The general difference between the laminography and limited-angle CT reconstructions of the Lego sample is the homogeneity of the artefacts in the xy plane, which can be directly attributed to the difference in the shape of the region of missing information in Fourier space for the two different methods. Deciding what method produces the best reconstruction would in general depend on the sample that was being scanned, and the shape of the features of interest. However in this case, it is clear that the sample is more faithfully imaged by the laminography method, as the uniformly distributed
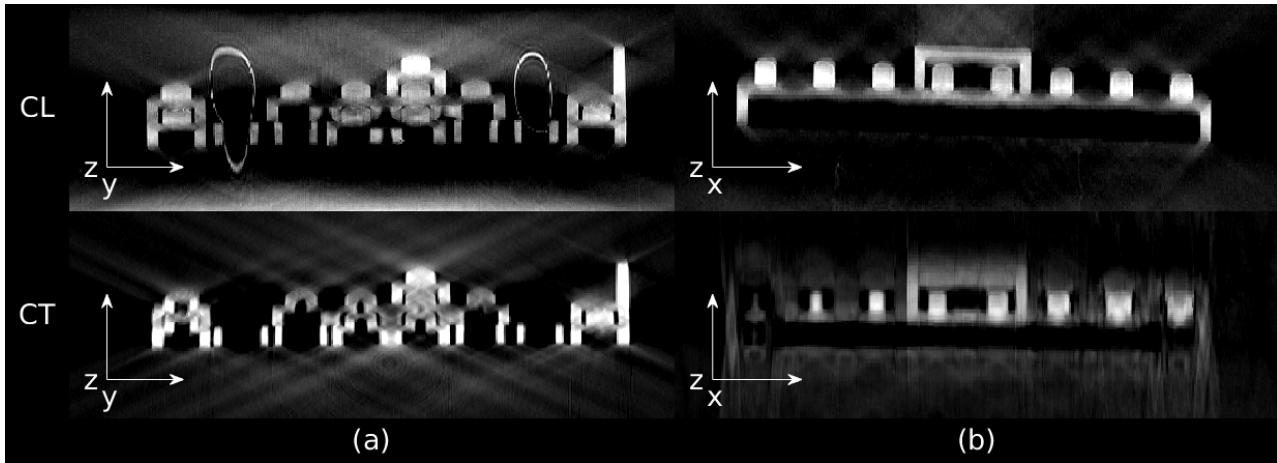
Figure 14. Cross-sections through the reconstructed volume in the *yz* plane, column (a), and the *xz* plane, column (b), for both the CL and CT methods.

artefacts do not obscure the features as much as the limited-angle CT case. Neither method produces an ideal reconstruction of the object in the *yz* and *xz* planes, but this is to be expected since both cases use incomplete data. However, edges in the *xz* plane that are completely lost by limited-angle CT are more sharply reproduced by the laminography method.

An advantage of laboratory-based CL over limited-angle CT is the higher achievable magnification, which translates directly into higher resolution. The geometry of laminography could allow part of the sample to rotate below the x-ray source, which would mean that a much smaller source-to-object distance could be achieved with laminography when compared to limited-angle CT. This higher magnification also means that CL could be well-suited to region-of-interest (ROI) scans where only a small area of the sample is scanned at higher resolution, for example a small impact-damaged region in a large composite panel. For an ROI scan to be successful, it is important to design a mount that keeps the ROI in the centre of the image at all projection angles. This is a technical challenge not just for CL scans but also CT in general.

An area for further development is the methodology for determining the parameters used in the artefact correction. Currently, the methods discussed to determine geometrical parameters such as the source-to-object distance and tilt angle are associated with some uncertainty. When using equation (7) to determine the source-to-object distance, an uncertainty arises from the measurement of the width of the sample on the projection image because of overlap of shapes in the projection image. This obscures the edges of the sample and means there is a range of possible measurements for the sample width. The source-to-object distance measured using the method discussed in this work was found to be (313 ± 8) mm. Multiple reconstructions in this range found a source-to-object distance of 315 mm to be the optimal value. Although this technique does provide a valid range of possible source-to-object distances in which to try, testing all the different distances in the range is time-consuming. It may be better to calculate the distance using a projection of a single component test object, without any overlapping features, to reduce the measurement error.

In addition, a similar trial-and-error based method was used in this work to determine the COR correction. Again, to improve the speed by which an optimal reconstruction is obtained, it could be beneficial to use a systematic approach, for example the technique discussed in [39].

Another area for development is the choice of reconstruction algorithm. The CGLS algorithm used in this work is fast which makes it ideal for use in a proof-of-concept study, however does not implement features such as non-negativity which can improve image quaility. The effect of non-negativity as well as edge-preserving regularisation techniques such as total variation regularisation [40–43] should be investigated.

6. Conclusions

It has been shown using a simple test object that laboratory-based x-ray CL can be implemented on a conventional x-ray CT scanner and that useful reconstructions can be obtained. Further, in agreement with the literature, CL was found to produce reconstructions of superior quality in the plane parallel to the object face, when compared to limited-angle CT with a specifically designed planar Lego test sample. This is the first step in the development of a laboratory-based CL scanning routine. Future work will include application of the CL setup to investigate a variety of samples for which standard CT is not a viable option, such as the case of damage in composite panels, which due to their planar geometry are difficult to image on a conventional CT system. This will involve region-of-interest scanning for increased spatial resolution, as enabled by the larger magnification possible in the CL configuration.

To achieve this a new mount would need to be designed allowing larger planar objects to be successfully scanned. Larger objects would require a sturdier mount than the polystyrene mount used in this proof-of-concept study.

The characterisation of geometric misalignment artefacts performed in this work was essential to eliminating artefacts observed in the raw Lego reconstruction. Each of the artefacts are very different in nature and our characterisation will enable other users to identify the necessary corrections

for their own laminography systems. To make the developed CL setup available for routine use, it would be useful to automate the process of determining optimal correction parameters by developing a robust calibration routine. This would eliminate the need for time-consuming manual optimisation. Such calibration routines have been extensively studied in CT [44, 45]. Additionally, a reconstruction algorithm that implements non-negativity or edge-preserving regularisation could also be used in future systems instead of CGLS to improve the image quality.

Successfully implementing laboratory-based x-ray CL on a Lego sample is a large step towards more widely available high-quality 3D imaging of large planar objects whose dimensions prevent the use of conventional CT. The fact that no specialist equipment was used beyond that which is already required for a standard CT scan is a significant advantage.

Acknowledgments

ORCID iDs

S L Fisher https://orcid.org/0000-0003-1062-4266
J S Jørgensen https://orcid.org/0000-0001-9114-754X
P Gajjar https://orcid.org/0000-0001-7109-708X
W R B Lionheart https://orcid.org/0000-0003-0971-4678
P J Withers https://orcid.org/0000-0002-1946-5647

References

[1] Ritman E L 2011 Current status of developments and applications of micro-CT *Annu. Rev. Biomed. Eng.* **13** 531–52

[2] Stock S R 1999 X-ray microtomography of materials *Int. Mater. Rev.* **44** 141–64

[3] Stock S R 2008 Recent advances in x-ray microtomography applied to materials *Int. Mater. Rev.* **53** 129–81

[4] Cnudde V and Boone M N 2013 High-resolution x-ray computed tomography in geosciences: a review of the current technology and applications *Earth-Sci. Rev.* **123** 1–17

[5] Legrand S, Vanmeert F, Van der Snickt G, Alfeld M, De Nolf W, Dik J and Janssens K 2014 Examination of historical paintings by state-of-the-art hyperspectral imaging methods: from scanning infra-red spectroscopy to computed x-ray laminography *Heritage Sci.* **2** 13

[6] Helfen L, Myagotin A, Mikulk P, Pernot P, Voropaev A, Elyyan M, Michiel M D, Baruchel J and Baumbach T 2011 On the implementation of computed laminography using synchrotron radiation *Rev. Sci. Instrum.* **82** 063702

[7] Houssaye A, Xu F, Helfen L, Buffrénil V D, Baumbach T and Tafforeau P 2011 Three-dimensional pelvis and limb anatomy of the Cenomanian hind-limbed snake *Eupodophis descouensi* (Squamata, Ophidia) revealed by synchrotron-radiation computed laminography *J. Vertebrate Paleontology* **31** 2–7

[8] Borstnar G, Mavrogordato M N, Helfen L, Sinclair I and Spearing S M 2015 Interlaminar fracture micro-mechanisms in toughened carbon fibre reinforced plastics investigated via synchrotron radiation computed tomography and laminography *Composites* A **71** 176–83

[9] Helfen L, Baumbach T, Mikulk P, Kiel D, Pernot P, Cloetens P and Baruchel J 2005 High-resolution three-dimensional imaging of flat objects by synchrotron-radiation computed laminography *Appl. Phys. Lett.* **86** 071915

[10] O'Brien N S, Boardman R P, Sinclair I and Blumensath T 2016 Recent advances in x-ray cone-beam computed laminography *J. X-Ray Sci. Technol.* **24** 691–707

[11] Xu F, Helfen L, Suhonen H, Elgrabli D, Bayat S, Reischig P, Baumbach T and Cloetens P 2012 Correlative nanoscale 3D imaging of structure and composition in extended objects *PLoS One* **7** 1–6

[12] Helfen L, Myagotin A, Pernot P, DiMichiel M, Mikulìk P, Berthold A and Baumbach T 2006 Investigation of hybrid pixel detector arrays by synchrotron-radiation imaging *Nucl. Instrum. Methods Phys. Res.* A **563** 163–66 (*Proc. 7th Int. Workshop on Radiation Imaging Detectors*)

[13] Helfen L, Xu F, Suhonen H, Cloetens P and Baumbach T 2013 Laminographic imaging using synchrotron radiation challenges and opportunities *J. Phys.: Conf. Ser.* **425** 192025

[14] Hoshino M, Uesugi K, Takeuchi A, Suzuki Y and Yagi N 2011 Development of an x-ray micro-laminography system at SPring-8 *AIP Conf. Proc.* **1365** 250–3

[15] Cheng Y, Altapova V, Helfen L, Xu F, dos Santos Rolo T, Vagovič P, Fiederle M and Baumbach T 2013 Multi-contrast computed laminography at ANKA light source *J. Phys.: Conf. Ser.* **463** 012038

[16] Zuber M, Laaß M, Hamann E, Kretschmer S, Hauschke N, van de Kamp T, Baumbach T and Koenig T 2017 Augmented laminography, a correlative 3D imaging method for revealing the inner structure of compressed fossils *Sci. Rep.* **7** 41413

[17] Xu F, Helfen L, Moffat A J, Johnson G, Sinclair I and Baumbach T 2010 Synchrotron radiation computed laminography for polymer composite failure studies *J. Synchrotron Radiat.* **17** 222–6

[18] Krug K *et al* 2008 Relics in medieval altarpieces? Combining x-ray tomographic, laminographic and phase-contrast imaging to visualize thin organic objects in paintings *J. Synchrotron Radiat.* **15** 55–6

[19] O'Brien N, Mavrogordato M, Boardman R, Sinclair I, Hawker S and Blumensath T 2016 Comparing cone beam laminographic system trajectories for composite ndt *Case Stud. Nondestruct. Test. Eval.* **6** 56–61

[20] Wood C, O'Brien N, Denysov A and Blumensath T 2018 Computed laminography of CFRP using an x-ray cone beam and robotic sample manipulator systems *IEEE Trans. Nuclear Science* **65** 1384–93

[21] Blumensath T, O'Brien N and Wood C 2017 Calibrating cone-beam tomography systems with generic trajectories *IEEE Trans. Nucl. Sci.* (submitted)

[22] Tuy H K 1983 An inversion formula for cone-beam reconstruction *Soc. Ind. Appl. Math.* **43** 546–52

[23] Finch D 1985 Cone beam reconstruction with sources on a curve *SIAM J. Appl. Math.* **45** 665–73

[24] Gajjar P 2017 IPC Quick Start Guide *Technical Report* The University of Manchester and Nikon Meterology

[25] Gajjar P, Jørgensen J S, Godinho J R A, Johnson C G, Ramsey A and Withers P J 2018 New software protocols for enabling laboratory based temporal CT *Rev. Sci. Instrum.* **89** 093702

[26] Olivera S, Muralidhara H B, Venkatesh K, Gopalakrishna K and Vivek C S 2016 Plating on acrylonitrile–butadiene–styrene (ABS) plastic: a review *J. Mater. Sci.* **51** 3657–74

[27] Kelly M J and Dean M C 2016 A specific nanomanufacturing challenge *Nanotechnology* **27** 112501

[28] Feldkamp L A, Davis L C and Kress J W 1984 Practical cone beam algorithm *Opt. Soc. Am.* **1** 612–9

[29] Yang M, Wang G and Liu Y 2010 New reconstruction method for x-ray testing of multilayer printed circuit board *Opt. Eng.* **49** 056501

[30] Bleichrodt F, van Leeuwen T, Palenstijn W J, van Aarle W, Sijbers J and Batenburg K J 2016 Easy implementation of advanced tomography algorithms using the ASTRA toolbox with spot operators *Numer. Algorithms* **71** 673–97

[31] Hestenes M R and Stiefel E 1952 Methods of conjugate gradients for solving linear systems *J. Res. Natl Bur. Stand.* **49** 409–36

[32] Gilbert P 1972 Iterative methods for the three-dimensional reconstruction of an object from projections *J. Theor. Biol.* **36** 105–16

[33] Hansen P C and Jørgensen J S 2018 AIR Tools II: algebraic iterative reconstruction methods, improved implementation *Numer. Algorithms* **79** 107–37

[34] Hansen P C 2010 *Discrete Inverse Problems and Algorithms* (Philadelphia, PA: SIAM)

[35] van Aarle W, Palenstijn W J, Cant J, Janssens E, Bleichrodt F, Dabravolski A, Beenhouwer J D, Batenburg K J and Sijbers J 2016 Fast and flexible x-ray tomography using the ASTRA toolbox *Opt. Soc. Am.* **24** 129–47

[36] van Aarle W, Palenstijn W J, Beenhouwer J D, Altantzis T, Bals S, Batenburg K J and Sijbers J 2015 The ASTRA toolbox: a platform for advanced algorithm development in electron tomography *Ultramicroscopy* **157** 35–47

[37] Davis G R and Elliott J C 2006 Artefacts in x-ray microtomography of materials *Mater. Sci. Technol.* **22** 1011–8

[38] Xu F, Helfen L, Baumbach T and Suhonen H 2012 Comparison of image quality in computed laminography and tomography *Opt. Soc. Am.* **20** 794–806

[39] Yang M, Li Z, Liang L, Li X, Liu W and Gui Z 2014 Automatic measurement of rotation center for laminography scanning systems without dedicated phantoms *J. Electron. Imaging* **23** 053018

[40] Rudin L I, Osher S and Fatemi E 1992 Nonlinear total variation based noise removal algorithms *Physica* D **60** 259–68

[41] Jensen T L, Jørgensen J H, Hansen P C and Jensen S H 2011 Implementation of an optimal first-order method for strongly convex total variation regularization *BIT Numer. Math.*

[42] Sidky E Y and Pan X 2008 Image reconstruction in circular cone-beam computed tomography by constrained, total-variation minimization *Phys. Med. Biol.* **53** 4777–807

[43] Bian J, Siewerdsen J H, Han X, Sidky E Y, Prince J L, Pelizzari C A and Pan X 2010 Evaluation of sparse-view reconstruction from flat-panel-detector cone-beam CT *Phys. Med. Biol.* **55** 6575–99

[44] Ferrucci M, Leach R K, Giusca C, Carmignato S and Dewulf W 2015 Towards geometrical calibration of x-ray computed tomography systems—a review *Meas. Sci. Technol.* **26** 092003

[45] Yang K, Kwan A L C, Miller D F and Boone J M 2006 A geometric calibration method for cone beam CT systems *Med. Phys.* **33** 1695–706